nature nanotechnology

ARTICLES

PUBLISHED ONLINE: 27 JUNE 2016 | DOI: 10.1038/NNANO.2016.110

Perovskite energy funnels for efficient light-emitting diodes

Mingjian Yuan[1‡], Li Na Quan[1,2‡], Riccardo Comin[1], Grant Walters[1], Randy Sabatini[1], Oleksandr Voznyy[1], Sjoerd Hoogland[1], Yongbiao Zhao[1,3], Eric M. Beauregard[1], Pongsakorn Kanjanaboos[1†], Zhenghong Lu[3], Dong Ha Kim[2*] and Edward H. Sargent[1*]

Organometal halide perovskites exhibit large bulk crystal domain sizes, rare traps, excellent mobilities and carriers that are free at room temperature—properties that support their excellent performance in charge-separating devices. In devices that rely on the forward injection of electrons and holes, such as light-emitting diodes (LEDs), excellent mobilities contribute to the efficient capture of non-equilibrium charge carriers by rare non-radiative centres. Moreover, the lack of bound excitons weakens the competition of desired radiative (over undesired non-radiative) recombination. Here we report a perovskite mixed material comprising a series of differently quantum-size-tuned grains that funnels photoexcitations to the lowest-bandgap light-emitter in the mixture. The materials function as charge carrier concentrators, ensuring that radiative recombination successfully outcompetes trapping and hence non-radiative recombination. We use the new material to build devices that exhibit an external quantum efficiency (EQE) of 8.8% and a radiance of 80 W sr^{-1} m^{-2}. These represent the brightest and most efficient solution-processed near-infrared LEDs to date.

Perovskite solar cells have recently reached certified power conversion efficiencies of 20.1%[1] due to their superior charge carrier mobilities and the low densities of deep trap states[2–4]. The materials also exhibit outstanding optical properties[5] (including wide colour tunability[6]) that make them highly relevant to light emission applications. Bulk and quantum dot perovskites[7–9] have featured in impressive optically pumped lasers[10–12] and LEDs[13–17].

As excitons have low binding energies (9–60 meV; refs 18,19) in $CH_3NH_3PbI_3$ perovskites, the charge carriers are free (instead of forming bound excitons) at room temperature[20]. The photoluminescence quantum yield (PLQY) of $CH_3NH_3PbI_3$ perovskites therefore depends on the excitation intensity, and reaches a higher value at high excitation photon fluences where radiative bimolecular recombination dominates. Trap-mediated non-radiative recombination dominates under weak excitation, resulting in relatively low PLQY[21,22].

In LED applications, the injected carrier density at typical applied biases is too low to fill the trap states completely. As a result, under normal operating conditions the actual PLQY is low compared with high-excitation-density values[22,23]. The performance of perovskite LEDs has been severely curtailed by the low radiative efficiency of the active medium under device operating conditions.

To improve LED performance, perovskite films are typically engineered to be thin (~20 nm) to both confine the injected charges and maximize the carrier density[24]. However, as pinholes are unavoidable in such thin films, the average EQEs for perovskite LEDs have, until recently, remained moderate[25,26]. A new strategy was developed recently to spatially confine the injected charges within $CH_3NH_3PbBr_3$ nanograins, increasing the probability of dissociated excitons regaining their bound form. The reduced grain size thereby increased the radiative recombination rate, resulting in an enhanced PLQY and an impressive EQE of 8.53% in the visible region[5]. Although this strategy was very successful in bromide perovskites, the iodide $CH_3NH_3PbI_3$ possesses an exciton binding energy that is three times lower[21] and spatial confinement therefore has yet to produce the much-needed increase in the PLQY for infrared-emitting perovskites (Supplementary Fig. 25).

Further improving the efficiency of radiative recombination under low-level injection is an important route to more efficient perovskite LEDs[27]. Two-dimensional (2D) layered perovskites[28,29] provide one means to form excitons at room temperature, with the largest exciton binding energy reaching an impressive $E_b \approx 320$ meV (ref. 30). However, strong luminescence has so far only been observed from these materials at liquid nitrogen temperatures. The lack of efficient luminescence at room temperature is still not well understood, but has been tentatively assigned to the thermal quenching of excitons[31,32].

We sought to explore whether increasing the average number of layers $\langle n \rangle$ that make up the average dimensionally tuned perovskite in a solid-state material could be used as a means to enhance the PLQY. $\langle n \rangle$ is equal to the number of PbI_6 monolayer sheets within a layer (Fig. 1a). Both E_b and the bandgap of these multilayered quasi-2D perovskites ($\langle n \rangle > 1$) are lower than those of 2D perovskites ($n = 1$), as expected from the weaker quantum confinement as the number of layers increases.

We synthesized multilayered quasi-2D perovskite compounds by incorporating the bulky cation phenylethylammonium (PEA = $C_8H_9NH_3$). PEA possesses a large ionic radius that does not fit into the corner-sharing lead halide octahedral 3D framework; it thereby causes the 3D perovskite architecture to separate into layers[33]. The thickness of each unit cell of quasi-2D perovskites will expand via the incorporation of additional CH_3NH_3 cations (Fig. 1a). In this way, we achieve dimensional modulation by adjusting the ratio of methylammonium iodide (CH_3NH_3I, MAI) to PEA iodide (PEAI). This yields grains with the composition

[1]Department of Electrical and Computer Engineering, University of Toronto, 35 St George Street, Toronto, Ontario M5S 1A4, Canada. [2]Department of Chemistry and Nano Science, Ewha Womans University, 52 Ewhayeodae-gil, Seodaemun-gu, Seoul 03760, Korea. [3]Department of Materials Science and Engineering, University of Toronto, 184 College Street, Toronto, Ontario M5S 3E4, Canada. †Present address: Materials Science and Engineering, Faculty of Science, Mahidol University, 272 Rama 6 Road, Ratchathewi District, Bangkok 10400, Thailand. ‡These authors contributed equally to this work.
*e-mail: ted.sargent@utoronto.ca; dhkim@ewha.ac.kr

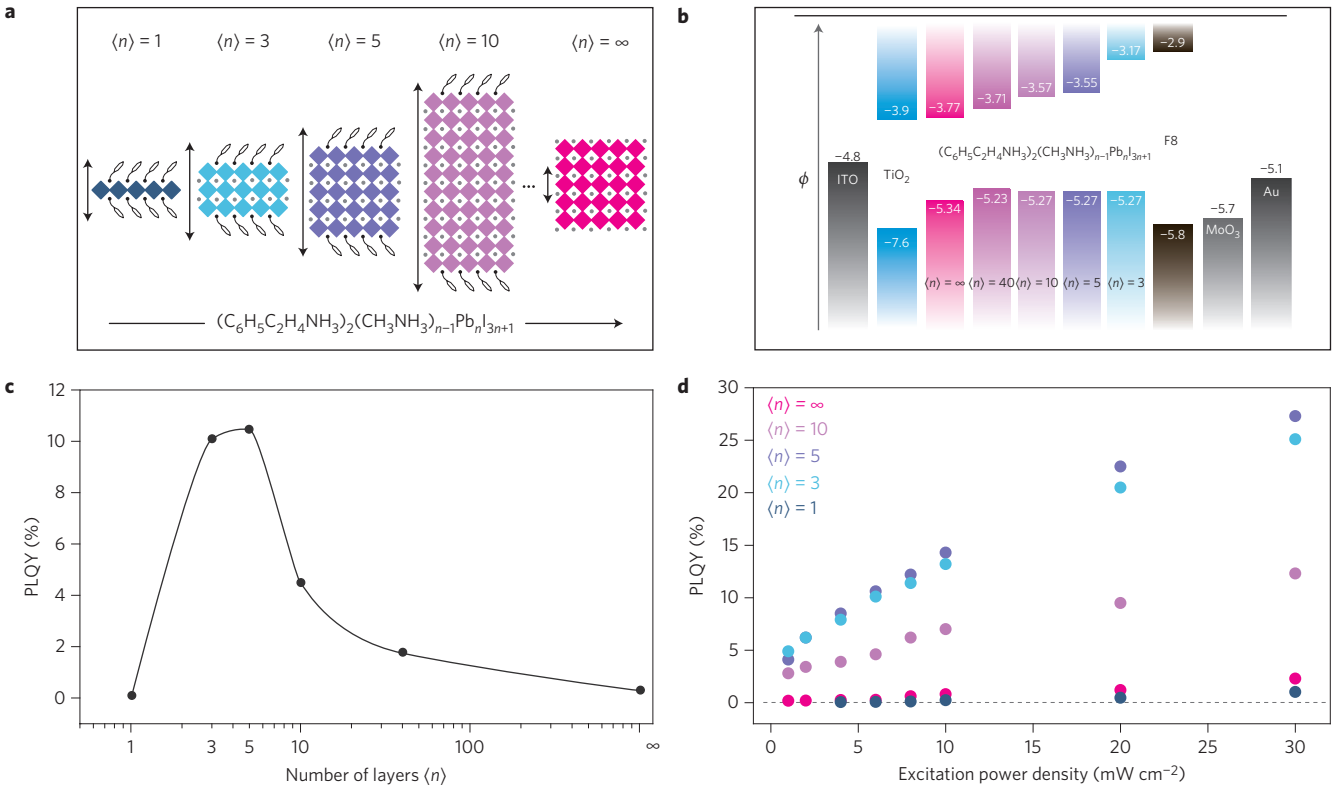

Figure 1 | Unit cell structure, electronic bandstructure and photoluminescent properties of quasi-2D perovskites. a, Unit cell structure of $(C_8H_9NH_3)_2(CH_3NH_3)_{n-1}Pb_nI_{3n+1}$ perovskites with different $\langle n\rangle$ values, showing the evolution of dimensionality from 2D ($n = 1$) to 3D ($n = \infty$). **b**, Electronic band structure of perovskites with different $\langle n\rangle$ values, combined with the band structure of ITO, TiO_2, F8, MoO_3 and the Au electrode. ϕ, electric potential. **c**, Summary of the PLQY for perovskite films with different $\langle n\rangle$ values at a low excitation intensity (6 mW cm^{-2}). **d**, Evolution of the PLQY with increasing excitation intensity for perovskites with different $\langle n\rangle$ values. The data show a steeper and earlier (lower threshold intensity) rise in PLQY for quasi-2D perovskites compared with 2D and 3D perovskites.

$PEA_2(CH_3NH_3)_{n-1}Pb_nI_{3n+1}$, with the average grain comprising $\langle n\rangle$ sheets of PbI_6 (Supplementary Table 1).

Structure and photoluminescence of quasi-2D perovskites

We obtained the desired quasi-2D perovskite films through a stoichiometric reaction between PbI_2, MAI and PEAI, followed by one-step spin casting. X-ray diffraction (XRD) was used to monitor the structural evolution from 3D to quasi-2D perovskites. Thin-film XRD patterns revealed no significant differences among the samples, consistent with a preferential orientation of crystallites in each sample[34]. We therefore pursued low-angle Bragg reflection, which we expected to reveal layered perovskites with their expanded unit cell[35]. We produced a powder from each film, thereby disturbing the preferential orientation, and found a notable difference in the XRD patterns of unoriented quasi-2D versus 3D perovskite samples (Supplementary Fig. 1). In the case of quasi-2D perovskites, a series of Bragg reflections at low angles (2θ <10°) was observed, revealing the vertical growth of the unit cell, which is indicative of lead iodide $\langle n\rangle$-layer perovskite sheets[36]. X-ray photoelectron spectroscopy (XPS) was used to determine the stoichiometry present at the surface of quasi-2D perovskite films. XPS core-level photoemission spectra of iodine 3*d* and nitrogen 1*s* are shown in Supplementary Fig. 12. The result revealed I:Pb and N:Pb ratios that gradually increased with decreasing $\langle n\rangle$ values. The trend is consistent with the nominal molar ratio of the precursors.

We determined the position of the valence band maxima (VBM) of these quasi-2D perovskites using ultraviolet photoelectron spectroscopy (UPS). The conduction band minima (CBM) were then indirectly calculated by subtracting the optical bandgap (Supplementary Figs 11 and 14). The films exhibited a similar value of VBM[37]; however, the CBM gradually increases with decreasing $\langle n\rangle$ values (Fig. 1b). This phenomenon is similar to that observed in the quantum size effect tuning in colloidal quantum dots[38].

PL spectra were also used to track the dimensional modulation. Lower $\langle n\rangle$ value materials exhibit the expected higher electronic bandgap. The trends for the PL emission peak and E_b (extracted from the temperature-dependent PL data presented in the Supplementary Information) are summarized in Supplementary Figs 2 and 3. As expected, decreasing dimensionality results in an increase in both the bandgap and E_b due to the stronger dielectric confinement. The trends in E_b, consistent with previous results[30], further confirmed that different grain thickness values were indeed achieved through control over the stoichiometry of the bulk-incorporating (MA) versus the surface-terminating (PEA) organic cations.

The PLQY as a function of $\langle n\rangle$ at a low excitation intensity (6 mW cm^{-2}) for different perovskites is summarized in Fig. 1c. The 3D $CH_3NH_3PbI_3$ perovskite films exhibits low PLQY (~0.2%), a fact that we attribute to a dominance of trap-mediated non-radiative recombination, consistent with previous reports[22]. Similarly, the 2D perovskite compound, PEA_2PbI_4 ($n = 1$), also exhibits low photoluminescence in films (PLQY <0.1%), again in agreement with previous studies[28,31].

Strikingly, quasi-2D perovskites with $\langle n\rangle = 3$ and $\langle n\rangle = 5$ show a substantially more intense photoluminescence: their respective PLQY values reach 10.1 and 10.6% under the same low (6 mW cm^{-2}) excitation intensities for which the PLQY of 3D materials is negligible. We also explored PL intensity as a function of the excitation intensity for different $\langle n\rangle$ perovskite films (Fig. 1d and Supplementary Fig. 9)

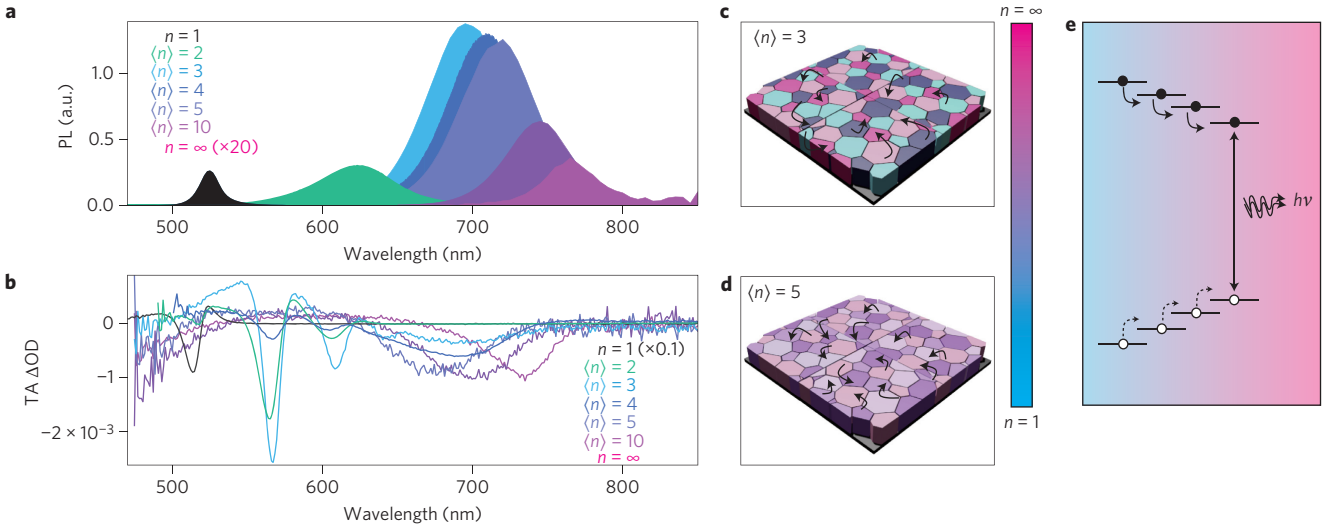

Figure 2 | Carrier funnelling in quasi-2D perovskite solids. a, Steady-state PL spectra for perovskites with different ⟨*n*⟩ values. **b**, TA spectra for perovskites with different ⟨*n*⟩ values. They track the recovery of the transient bleach of the bandedge absorption as photoexcited carriers populate various states and then ultimately transfer out of, or recombine from, those states. OD, optical density. **c**, The carrier transfer process in <*n*> = 3 perovskite. **d**, Carrier transfer process in <*n*> = 5 perovskite. **e**, Multi-phase perovskite materials $PEA_2(CH_3NH_3)_{n-1}Pb_nI_{3n+1}$ channel energy across an inhomogeneous energy landscape, concentrating carriers to smallest bandgap emitters. The arrows represent the carrier transfer process.

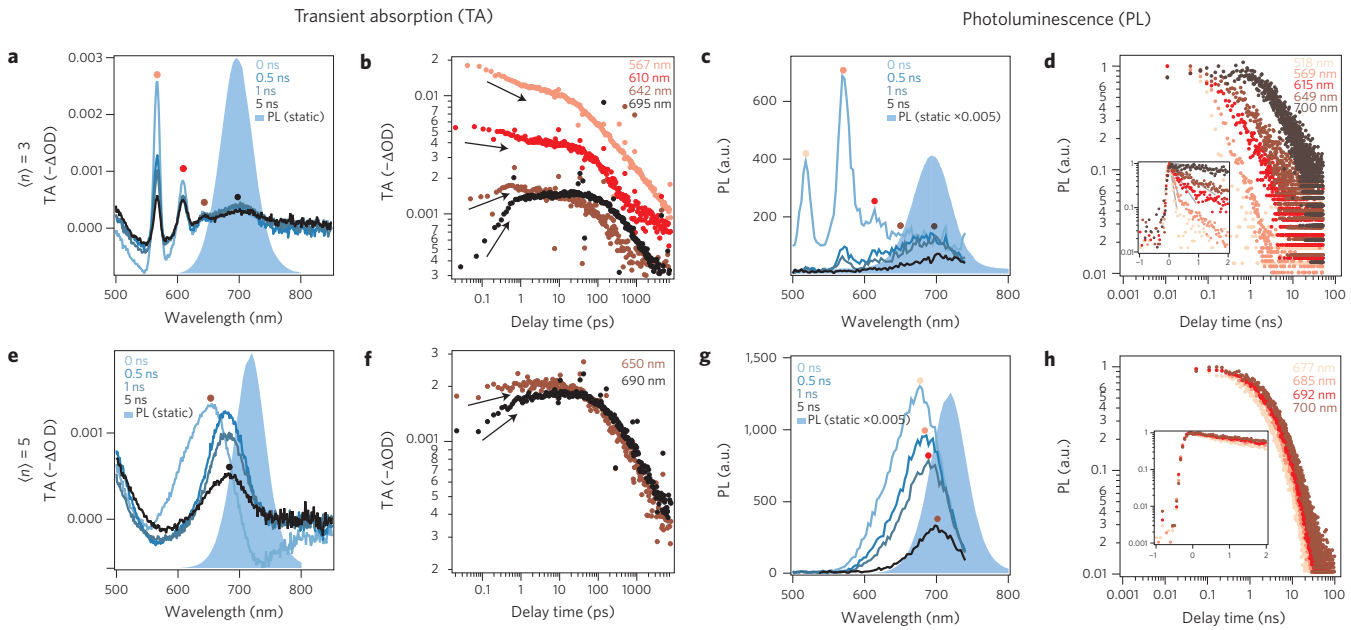

Figure 3 | TA and time-resolved PL spectra for quasi-2D perovskite, ⟨*n*⟩ = 3 and ⟨*n*⟩ = 5. a, TA spectra for an ⟨*n*⟩ = 3 perovskite at different timescales show that the relative intensity of the four bleaching peaks evolves on times. **b**, TA spectra for an ⟨*n*⟩ = 3 perovskite that probed selected wavelengths corresponding to the distinct bleaching lines as a function of delay time. **c**, PL for an ⟨*n*⟩ = 3 perovskite at distinct timescales. **d**, PL decay curve probed at selected wavelengths for an ⟨*n*⟩ = 3 perovskite. The inset figure shows further detail: PL decay at shorter wavelengths exhibits a bi-exponential behaviour, where the fast decay can be attributed to an intraband relaxation pathway from the carrier funnelling process. In contrast, the smallest bandgap species exhibits a single timescale associated with recombination alone. **e**, TA spectra for <*n*> = 5 perovskite at different timescales. **f**, TA spectra for <*n*> = 5 perovskite at different wavelengths as a function of delay time. **g**, PL spectra for <*n*> = 5 perovskite at different timescales. **h**, Time-resolved spectra for <*n*> = 5 perovskite at selected wavelengths.

and found a steeper and earlier (lower threshold intensity) rise in PLQY for quasi-2D perovskites as a function of the excitation intensity regime.

A possible initial explanation for the superior performance of the quasi-2D perovskites is a great excitonic character of the photocharges. However, the position of the PL emission spectra of the quasi-2D perovskites closely approaches that of the 3D ($CH_3NH_3PbI_3$) materials. This suggests similar free (unconfined) behaviour of the photocarriers in the principal light-emitting media in the ⟨*n*⟩ = 3 and ⟨*n*⟩ = 5 quasi-2D perovskite solids.

Transient dynamics

We therefore sought deeper insight into the dynamics of photocarriers in the quasi-2D perovskites compared with controls. Transient absorption (TA) and time-resolved PL spectroscopy enable the characterization of carrier transport and the recombination

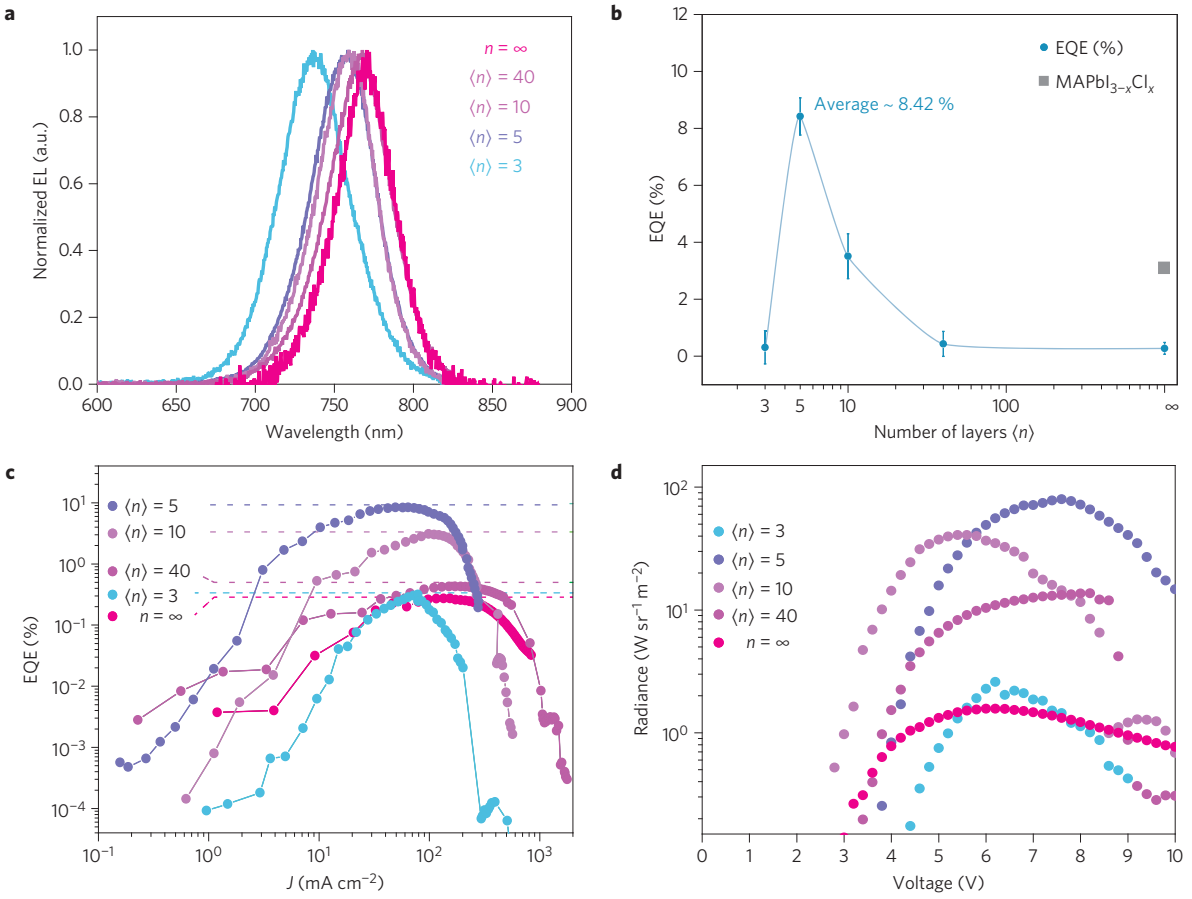

Figure 4 | EL and LED device performance of quasi-2D perovskites. a, EL spectra of perovskites with different ⟨*n*⟩ values. **b**, Summary of the device EQE for perovskites with different ⟨*n*⟩ values compared with the best reported device EQE for an iodide-based 3D perovskite LED[26]. The average EQE for ⟨*n*⟩ = 3 perovskite LEDs is 8.42%, based on more than 30 devices. Error bars represent the standard deviation of several devices. **c**, EQE versus *J* characteristics of perovskites with different ⟨*n*⟩ values. **d**, Summary of the device radiance versus voltage characteristics of perovskites with different ⟨*n*⟩ values.

processes at ultrafast timescales, thus providing a view into the transfer and recombination dynamics of photogenerated charges. Time-resolved differential absorption spectra track the recovery of the transient bleach of the bandedge absorption as photoexcited carriers (generated using a laser pulse with a 400 nm wavelength, 150 fs duration and 4 μJ cm^{-2} excitation) populate various states and then ultimately transfer out of, or recombine from, such states.

Intriguingly, we observed four distinctive bleach peaks in the TA spectrum for ⟨*n*⟩ = 3 quasi-2D perovskite films (Fig. 2b and Supplementary Fig. 16). The peak positions of these transitions are in good agreement with peaks in the steady-state absorption spectrum (Supplementary Fig. 5). These results suggest that the quasi-2D perovskite films are not single-phase, but rather consist of a collection of grains exhibiting a variety of ⟨*n*⟩ values. These observations led us to believe that typical films having an expected value of ⟨*n*⟩ = 3 contained ⟨*n*⟩ = 2, 3, 4 and 5 perovskite phases in significant proportions. The fact that the steady-state PL spectrum of the ⟨*n*⟩ = 3 perovskite film reflects the smallest bandgap component already indicates that photoexcitation transfer is at play in these materials. Similar phenomena were observed in the ⟨*n*⟩ = 5 quasi-2D perovskite films, where an inhomogeneously broadened bleaching peak was observed around 700 nm. The bandgap approaches ⟨*n*⟩ independence (asymptotes) for large ⟨*n*⟩ (refs 39,40), hence the bleach peaks become indistinguishable and are manifest ultimately as peak broadening in the case of the large ⟨*n*⟩ materials.

TA spectra for ⟨*n*⟩ = 3 quasi-2D perovskite films (Fig. 3a and Supplementary Fig. 15a) further show that the relative intensities of the four bleaching peaks evolves on distinct timescales. Figure 3b and Supplementary Fig. 17a show the TA spectra probed at selected wavelengths corresponding to the distinct bleaching lines as a function of delay time.

Taken together, the data suggest a cascade[41,42] on the 100 fs–100 ps timescale from higher-energy states to lower-energy ones. After about 100 ps, the downward funnelling of energy is substantially complete and the remaining dynamics correspond to recombination in the lowest-energy inclusions.

Time-resolved PL measurements (Fig. 3c and Supplementary Fig. 15b) are in excellent agreement with the TA dynamics. Four different PL peaks were observed immediately following excitation; however, only the smallest bandgap PL emission can be observed following a 500 ps delay, reconfirming the funnelling/cascade picture seen in the TA results. The PL decay at shorter wavelengths exhibits a bi-exponential behaviour; we attribute the fast decay to an intraband relaxation pathway from the carrier funnelling process. In contrast, the smallest bandgap species (Fig. 3d and Supplementary Fig. 18b) exhibits a single timescale associated with recombination alone. We observed similar trends in ⟨*n*⟩ = 5 quasi-2D pervoskite films from both TA and time-resolved PL spectra (Fig. 3e–h and Supplementary Fig. 15c,d).

In summary, these studies of excitation dynamics suggest that the multiphased perovskite materials $PEA_2(MAI)_{n-1}Pb_nI_{3n+1}$ channel energy across an inhomogeneous energy landscape, concentrating carriers on smaller bandgap emitters. We posit that the high PLQY under low excitation is achieved because only the subset of trap states found inside the lowest-energy inclusions need to be

filled and there is an increased local excitation intensity within small bandgap grains, which is otherwise achievable only at higher excitation intensities in 3D perovskites.

We then investigated the film morphologies of quasi-2D perovskites with different $\langle n \rangle$ values. Excellent surface coverage was obtained for all quasi-2D perovskites (Supplementary Fig. 19) and the grain size was significantly reduced as $\langle n \rangle$ decreased (Supplementary Fig. 7). This reduction can be attributed to the PEAI molecules hindering crystal growth during crystal pinning[5]. High-resolution transmission electron microscopy (HRTEM) was employed to study the detailed crystalline features of these multigrain perovskites. The HRTEM images locally exhibit lattice fringes with characteristic d spacings that can be assigned to grains with different n values (Supplementary Fig. 8).

LED structure and performance

We then pursued the realization of enhanced-performance LEDs. Figure 4a shows the normalized electroluminescence (EL) spectra of quasi-2D perovskites with $\langle n \rangle = 3$, 5, 10, 40, as well as 3D perovskite. The EL devices are fabricated by stacking the following series of layers: indium tin oxide (ITO) as the bottom electrode, a thin layer of titanium dioxide (TiO_2) as an electron injection layer, the emissive layer ($PEA_2(MA)_{n-1}Pb_nI_{3n+1}$), the hole injecting layer poly(9,9′-dioctylfluorence) (F8) and molybdenum trioxide (MoO_3)/gold (Au) as the top electrode (Supplementary Fig. 24). By taking advantage of the solvent engineering fabrication process[43], we were able to achieve high-quality, ultra-smooth perovskite layers without pinholes for different $\langle n \rangle$ values.

The EQE of quasi-2D electroluminescent perovskite devices as a function of $\langle n \rangle$ value was also studied (Fig. 4b,c and Supplementary Fig. 21). The radiance versus voltage characteristics of the $\langle n \rangle = 5$ perovskite are shown in Fig. 4d. A clear turn-on of light emission can be observed at 3.8 V. A radiance of 80 W sr^{-1} m^{-2} was achieved at a current of 95 mA cm^{-2} when driven at 7.4 V. An average EQE of 8.4% (based on more than 30 devices) was achieved at 64 mA cm^{-2} and 6.4 V, determined on the basis of a Lambertian emission profile (Supplementary Fig. 20). The best-performing devices reach up to 8.8%. This gives an internal quantum efficiency (IQE) of 39%, calculated by IQE = $2n^2$EQE. We used the refractive index of glass ($n = 1.5$) in our estimation of IQE, as light is emitted isotropically into the glass substrate from the thin perovskite layer.

These results represent the most efficient and brightest solution-processed LED operating at near-infrared wavelengths reported so far, with an ~2.4× increase in peak EQE and an ~3× increase in peak radiance over the previous best-reported near-infrared perovskite EL devices. These results were achieved at an operating current density that is ~2.5× lower than in the best reports in the literature. The EQE rises rapidly with as the applied voltage and current density are increased, indicating that radiative bimolecular recombination dominates at higher excitation densities. Interestingly, we observe an increasing EQE and radiance with increasing perovskite layer thickness (Supplementary Figs 22 and 23). The EQE in $\langle n \rangle = 5$ perovskite films rises from 0.14% for 50 nm to 8.8% for 200 nm films, whereas the radiance increases from 1.2 to 80 W sr^{-1} m^{-2}. The improved EQE in thicker films is consistent with the trend of PLQY enhancement with increasing film thickness (Supplementary Fig. 10). The TA spectra for the $\langle n \rangle = 3$ perovskite with different film thicknesses further confirmed the more efficient energy transfer process in the thicker films compared with the thinner ones (Supplementary Fig. 4). In addition, thicker films provided a better surface coverage that significantly reduced leakage currents, also contributing to the improved performance.

The competition between non-radiative and radiative recombination governs the evolution of the EQE across perovskite devices with different $\langle n \rangle$ values. However, we register a drop in the EQE for $\langle n \rangle = 3$ despite the high PLQY. The low EQE is tentatively ascribed to a lower carrier injection efficiency arising from the large injection barrier between the electrode and small $\langle n \rangle$ (high bandgap) components.

Conclusions

In summary, the low efficiency of radiative recombination in EL devices based on $CH_3NH_3PbI_3$ perovskites motivated our exploration of new strategies to overcome this limitation. We found that multicomponent multilayered perovskite solids exhibit record-high PLQY under low excitation fluences. Dynamic studies enabled us to attribute this advance to the conveyance of excited carriers in a funnelling mechanism that provides carrier concentration[41,44], enabling more efficient radiative recombination and thereby overcoming the trap-mediated non-radiative recombination at much more practical fluences. As a direct result, the most efficient and brightest solution-processed LED operating at near-infrared wavelengths were produce, with an EQE of 8.8% and a corresponding radiance of 80 W sr^{-1} m^{-2}. The concept can be applied in visible emissions and white LEDs by tailoring the composition of the perovskites.

Methods

Methods and any associated references are available in the online version of the paper.

Received 9 December 2015; accepted 20 May 2016; published 27 June 2016

References

1. Yang, W. S. *et al.* High-performance photovoltaic perovskite layers fabricated through intramolecular exchange. *Science* **348,** 1234–1237 (2015).
2. Shi, D. *et al.* Low trap-state density and long carrier diffusion in organolead trihalide perovskite single crystals. *Science* **347,** 519–522 (2015).
3. Xing, G. *et al.* Long-range balanced electron-and hole-transport lengths in organic-inorganic $CH_3NH_3PbI_3$. *Science* **342,** 344–347 (2013).
4. Burschka, J. *et al.* Sequential deposition as a route to high-performance perovskite-sensitized solar cells. *Nature* **499,** 316–320 (2013).
5. Cho, H. *et al.* Overcoming the electroluminescence efficiency limitations of perovskite light-emitting diodes. *Science* **350,** 1222–1225 (2015).
6. Deschler, F. *et al.* High photoluminescence efficiency and optically pumped lasing in solution-processed mixed halide perovskite semiconductor. *J. Phys. Chem. Lett.* **5,** 1421–1426 (2014).
7. Schmidt, L. C. *et al.* Nontemplate synthesis of $CH_3NH_3PbBr_3$ perovskite nanoparticles. *J. Am. Chem. Soc.* **136,** 850–853 (2014).
8. D'Innocenzo,V., Kandada, A., Bastiani, M., Gandini, M. & Petrozza, A. Tuning the light emission properties by band gap engineering in hybrid lead halide perovskite. *J. Am. Chem. Soc.* **136,** 17730–17733 (2014).
9. Protesescu, L. *et al.* Nanocrystals of cesium lead halide perovskites ($CsPbX_3$, X = Cl, Br, and I): novel optoelectronic materials showing bright emission with wide color gamut. *Nano Lett.* **15,** 3692–3696 (2015).
10. Yakunin, S. *et al.* Low-threshold amplified spontaneous emission and lasing from colloidal nanocrystal of caesium lead halide perovskites. *Nature Commun.* **6,** 8056 (2015).
11. Xing, G. *et al.* Low-temperature solution-processed wavelength-tunable perovskite for lasing. *Nature Mater.* **13,** 476–480 (2014).
12. Zhang, Q., Ha, S. T., Liu, X., Sum, T. C. & Xiong, Q. Room-temperature near-infrared high-q perovskite whispering-gallery planar nanolasers. *Nano Lett.* **14,** 5995–6001 (2014).
13. Song, J. *et al.* Quantum dot light-emitting diodes based on inorganic perovskite cesium lead halides ($CsPbX_3$). *Adv. Mater.* **27,** 7162–7167 (2015).
14. Bade, S. *et al.* Fully printed halide perovskite light-emitting diodes with silver nanowire electrodes. *ACS Nano* **10,** 1795–1801 (2016).
15. Wong, A. B. *et al.* Growth and anion exchange conversion of $CH_3NH_3PbX_3$ nanorod arrays for light-emitting diodes. *Nano Lett.* **15,** 5519–5524 (2015).
16. Kim, Y. *et al.* Multicolored organic/inorganic hybrid perovskite light-emitting diodes. *Adv. Mater.* **27,** 1248–1254 (2015).
17. Sadhanala, A. *et al.* Blue-green color tunable solution processable organolead chloride–bromide mixed halide perovskites for optoelectronic applications. *Nano Lett.* **15,** 6095–6101 (2015).
18. Savenije, T. J. *et al.* Thermally activated exciton dissociation and recombination control the carrier dynamics in organometal halide perovskite. *J. Phys. Chem. Lett.* **5,** 2189–2194 (2014).
19. Yang, Y. *et al.* Observation of a hot-phonon bottleneck in lead-iodide perovskites. *Nature Photon.* **10,** 53–59 (2016).

20. Saba, M. *et al.* Correlated electron-hole plasma in organometal perovskites. *Nature Commun.* **5,** 5049 (2014).
21. Yang, Y. *et al.* Comparison of recombination dynamics in $CH_3NH_3PbBr_3$ and $CH_3NH_3PbI_3$ perovskite films: influence of exciton binding energy. *J. Phys. Chem. Lett.* **6,** 4688–4692 (2015).
22. Stranks, S. D. *et al.* Recombination kinetics in organic-inorganic perovskites: excitons, free charge, and subgap states. *Phys. Rev. Appl.* **2,** 034007 (2014).
23. Wu, X. *et al.* Trap states in lead iodide perovskites. *J. Am. Chem. Soc.* **137,** 2089–2096 (2015).
24. Tan, Z.-K. *et al.* Bright light-emitting diodes based on organometal halide perovskite. *Nature Nanotech.* **9,** 687–692 (2014).
25. Li, G. *et al.* Efficient light-emitting diodes based on nanocrystalline perovksite in a dielectric polymer matrix. *Nano Lett.* **15,** 2640–2644 (2015).
26. Wang, J. *et al.* Interfacial control toward efficient and low-voltage perovskite light-emitting diodes. *Adv. Mater.* **27,** 2311–2316 (2015).
27. Yamada, Y., Nakamura, T., Endo, M., Wakamiya, A. & Kanemitsu, Y. Photocarrier recombination dynamics in perovskite $CH_3NH_3PbI_3$ for solar cell applications. *J. Am. Chem. Soc.* **136,** 11610–11613 (2014).
28. Ishihara, T., Takahashi, J. & Goto, T. Optical properties due to electronic transitions in two-dimensional semiconductors $(C_nH_{2n+1}NH_3)_2PbI_4$. *Phys. Rev. B* **42,** 11099–11107 (1990).
29. Mitzi, D. B. in *Progress in Inorganic Chemistry* Vol. 48 (ed Karlin, K. D.) 1–121 (Wiley, 1999).
30. Hong, X., Ishihara, T. & Nurmikko, A. V. Dielectric confinement effect on excitons in PbI_4-based layered semiconductors. *Phys. Rev. B* **45,** 6961–6964 (1992).
31. Dou, L. *et al.* Atomically thin two-dimensional organic-inorganic hybrid perovskites. *Science* **349,** 1518–1521 (2015).
32. Chondroudis, K. & Mitzi, D. B. Electroluminescence from an organic-inorganic perovskite incorporating a quaterthiophene dye within lead halide perovskite layers. *Chem. Mater.* **11,** 3028–3030 (1999).
33. Kieslich, G., Sun, S. & Cheetham, A. K. An extended tolerance factor approach for organic–inorganic perovskites. *Chem. Sci.* **6,** 3430–3433 (2015).
34. Smith, I. C., Hoke, E. T., Solis-Ibarra, D., McGhee, M. D. & Karunadasa, H. I. A layered hybrid perovskite solar-cell absorber with enhanced moisture stability. *Angew. Chem. Int. Ed.* **126,** 11414–11417 (2014).
35. Cao, D. H., Stoumpos, C. C., Farha, O. K., Hupp, J. T. & Kanatzidis, M. G. 2D homologous perovskites as light-absorbing materials for solar cell applications. *J. Am. Chem. Soc.* **137,** 7843–7850 (2015).
36. Quan, L. *et al.* Ligand-stabilized reduced-dimensionality perovskites. *J. Am. Chem. Soc.* **138,** 2649–2655 (2016).
37. Miller, E. M. *et al.* Substrate-controlled band positions in $CH_3NH_3PbI_3$ perovskite films. *Phys. Chem. Chem. Phys.* **16,** 22122–22130 (2014).
38. Jasieniak, J., Califano, M. & Watkins, S. E. Size-dependent valence and conduction band-edge energies of semiconductor nanocrystals. *ACS Nano.* **5,** 5888–5902 (2011).
39. Tyagi, P., Arveson, S. M. & Tisdale, W. A. Colloidal organohalide perovskite nanoplatelets exhibiting quantum confinement. *J. Phys. Chem. Lett.* **6,** 1911–1916 (2015).
40. Sichert, J. A. *et al.* Quantum size effect in organometal halide perovskite nanoplatelets. *Nano. Lett.* **15,** 6521–6527 (2015).
41. Xu, F. *et al.* Efficient exciton funneling in cascaded PbS quantum dot superstructures. *ACS Nano.* **12,** 9950–9957 (2011).
42. Berggren, M., Dodabalapur, A., Slusher, R. E. & Bao, Z. Light amplification in organic thin films using cascade energy transfer. *Nature* **389,** 466–469 (1997).
43. Jeon, N. J. *et al.* Solvent engineering for high-performance inorganic–organic hybrid perovskite solar cells. *Nature Mater.* **13,** 897–903 (2014).
44. Gao, Y. *et al.* Enhanced hot-carrier cooling and ultrafast spectral diffusion in strongly coupled PbSe quantum-dot solids. *Nano Lett.* **15,** 6521–6527 (2015).

Acknowledgements

This publication is based in part on work supported by Award KUS-11-009-21, made by King Abdullah University of Science and Technology (KAUST), by the Ontario Research Fund Research Excellence Program, and by the Natural Sciences and Engineering Research Council (NSERC) of Canada. L. N. Quan and D. H. Kim acknowledge the financial support by National Research Foundation of Korea Grant funded by the Korean Government (2014R1A2A1A09005656). The authors thank R. Wolowiec and D. Kopilovic for their help during the course of the study.

Author contributions

M.Y., L.N.Q., R.C. and E.H.S. conceived the idea and proposed the experimental design. M.Y., L.N.Q., R.C., S.H., D.H.K. and E.H.S. performed and analysed XRD, UV absorption, PL lifetime, transient absorption and XPS measurements. M.Y., L.N.Q., P.K. and E.M.B performed the device fabrication. R.C., G.W and R.S. performed the TA and PL decay measurements. M.Y., L.N.Q., Y.Z. and Z.L. tested the devices. M.Y., L.N.Q., R.C., O.V. and E.H.S. co-wrote the manuscript. All authors read and commented on the manuscript.

Additional information

Supplementary information is available in the online version of the paper. Reprints and permissions information is available online at www.nature.com/reprints. Correspondence and requests for materials should be addressed to D.H.K. and E.H.S.

Competing financial interests

The authors declare no competing financial interests.

Methods

Perovskite film fabrication. Different dimensionality perovskite $[(PEA)_2(CH_3NH_3)_{n-1}Pb_nI_{3n+1}]$ solutions was prepared by dissolving stoichiometric quantities of lead iodide (PbI_2), methylammonium idodide (MAI) and PEAI in a dimethyl sulfoxide (DMSO)/γ-butyrolactone (1:1 volume ratio) mixture at 70 °C for 1 h with continuous stirring. The resulting solution was then filtered through a polytetrafluoroethylene (PTFE) filter (0.2 μm). The resulting solution was spin-coated onto the substrate via a two-step process at 1,000 r.p.m. and 5,000 r.p.m. for 10 s and 60 s, respectively. During the second spin step, 100 μl of chlorobenzene were poured onto the substrate. The resulting films were then annealed at 70 °C for 10 min to improve crystallization.

LED fabrication. The TiO_2 layer was deposited via atomic layer deposition (ALD) (Cambridge Savannah S100 ALD system) at 150 °C on oxygen-plasma-treated patterned ITO glass. The ~10 nm TiO_2 films were then further treated using aqueous solutions of $TiCl_4$ (40 mM). The series of different perovskite $[(C_6H_5C_2H_4NH_3)_2(CH_3NH_3)_{n-1}Pb_nI_{3n+1}]$ precursor solutions were spin-coated onto the TiO_2 via the single-step solvent engineering method described above. The hole-injecting polymer, poly (9,9′-dioctylfluorence), was dissolved in a chlorobenzene solution (10 mg ml^{-1}) and spin-coated onto the perovskite layer at 3,000 r.p.m for 60 s. MoO_3 (10 nm) and Au (100 nm) contacts were deposited by thermal evaporation and electron-beam deposition, respectively. Each ITO substrate (2.5 cm × 2.5 cm) was patterned with eight devices, each with an area of 0.0614 cm^2.

Atomic force microscopy measurements. The surface morphologies of the perovskite films with different $\langle n \rangle$ values were measured using ScanAsyst in air. The cantilever used is Scanasyst-air, a silicon tip on a nitride lever with spring constant of ~0.4 N m^{-1}. Samples were prepared in air under the same spin-coating conditions as the devices.

XPS measurements. XPS measurements were carried out in a Thermo Scientific K-Alpha system, with a 300 μm spot size, 75 eV pass energy and energy steps of 0.05 eV. All of the data are normalized according to the intensity of Pb for comparison between different samples.

UPS measurements. UPS characterization was carried out in an ultrahigh vacuum chamber with a base pressure below 5×10^{-9} mbar. The photon line width is ~250 meV and the minimum spot size is ~1 mm. He I photons (21.2 eV) were used to acquire the spectra at a normal emission level. The photoelectrons were collected by the SPHERA U7 hemispherical energy analyser with a 7-channel MCD detector in the constant analyzer energy mode. The E_b values shown with 10 meV precision should be rounded to the nearest 100 meV value in accordance with the overall energy resolution.

PL and EL measurements. PL was recorded using a Horiba Fluorolog system equipped with a single grating and a time-correlated single photon counting detector. For steady-state PL and PL excitation measurements, the excitation source is a monochromated Xe lamp. For time-resolved PL, we used an ultraviolet laser diode ($\lambda = 375$ nm); the overall time resolution as determined from the instrument response function is $\Delta t \sim 0.13$ ns. 2D time/wavelength PL maps were measured by collecting a series of individual time-resolved PL traces at different wavelengths with a spectrometer resolution of about 1 nm. The standard published method for calculating PLQY (ref. 45) was implemented using a Quanta-Phi integrating sphere coupled to the Fluorolog system with optic fibre bundles. The following settings were used for all quantum efficiency measurements: an excitation wavelength of 440 nm, bandpass values of 10 and 5 nm for the excitation and emission slits, respectively, step increments of 1 nm and integration times of 0.5 s per data point. These setting ensured that the spectra had high signal-to-noise ratios and provided excitation intensities in the range of 1–30 mW cm^{-2}. Excitation and emission spectra were collected with the sample directly in the excitation beam path, the sample offset from the beam path and the empty sphere, in accordance with the standard method. A calibrated neutral density filter with a known transmission was placed after the integrating sphere to measure the excitation intensity. The detector and integrating sphere were calibrated for spectral variance with a Newport white light source. For intensity-dependent photoluminescence measurements, the slit width on the Fluorolog monochromator was varied and the incident intensity was determined through measurements with an Ophir LasterStar Dual Channel Power and an energy meter using known dispersion relations for the monochromator. The EL was measured by applying a range of forward biases using a Keithley 2,410 Source Meter. The emitted light is collected and focused through a lens and connected to a visible spectrophotometer (Ocean Optics USB 2000+) using an optical fiber.

TA measurements. Femtosecond laser pulses were produced using a regeneratively amplified Yb:KGW laser at a 5 kHz repetition rate (Light Conversion, Pharos). The pump pulse was generated by passing a portion of the 1,030 nm probe pulse through an optical parametric amplifier (Light Conversion, Orpheus) with the second harmonic of the signal pulse selected for 400 nm light. Both the pump and probe pulses were directed into an optical bench (Ultrafast, Helios), where a white-light continuum was generated by focusing the 1,030 nm probe pulse through a sapphire crystal. The time delay (resolution ~350 fs) was adjusted by optically delaying the probe pulse, with time steps increasing exponentially. A chopper was used to block every other pump pulse and each probe pulse was measured by a charge-coupled device (CCD) after dispersion by a grating spectrograph (Ultrafast, Helios). Samples were prepared on a glass substrate and translated at 1 mm s^{-1} during the measurement. Pump fluences were kept at 4 μJ cm^{-2}. Kinetic traces were fitted to the convolution of the instrument response and a sum of the exponential decays. Time zero was allowed to vary with wavelength to account for the chirp of the probe.

LED characterization. Current density–voltage (J–V) characteristics were monitored via a computer-controlled Keithley 2,400 Source Meter. Front-face EL power output through ITO is measured using a calibrated Ophir PD300-3W silicon photodiode (active area: 1 cm^2) with a computer-interfaced Newport Multi-Function Optical Meter. The photodiode's active area is aligned with the emissive pixel and a diaphragm between the two prevents collection of waveguided EL from the glass substrate. The measurements were performed under a nitrogen atmosphere and in parallel with I-V measurements. Lambertian profile was used in the calculation of EQE and total radiance[45,46]. The peak EQE was determined as the number of emitted photons to the number of injected electrons. The measurement was calibrated using efficient OLED devices. The devices have been measured in two independent labs. A minimum of thirty devices were tested for each sample type.

EQE calculation. The EQE was determined as the ratio, per unit time, of the number of emitted photons to the number of injected electrons[46,47]:

$$\mathrm{EQE}(V) = \frac{N_{\mathrm{phot}(V)}e}{I(V)} * g * 100$$

where, $I(V)$ is the current passing through the device at an applied bias, V, $N_{\mathrm{phot}(V)}$ represents the number of emitted photons collected by the photodiode and the geometric factor, g, is the solid angle of the EL profile, assumed to be Lambertian, subtended by the photodiode, $\Omega = \pi/g$:

$$g = \frac{a^2 + L^2}{a^2}$$

where a is the diameter of the active area of the photodiode and L represent the distance between the emitting pixel and the active area. $N_{\mathrm{phot}(V)}$ was calculated from the photocurrent (I_{ph}) of the photodiode in response to the measured EL at each bias, accounting for the wavelength dependence of the responsivity, $R(\lambda)$, of the photodiode.

Radiance calculation. The emitted power P_{EL} can be expressed as[46,47]:

$$P_{\mathrm{EL}} = \int_{\lambda_i}^{\lambda_f} EL\,(\lambda)' \frac{hc}{\lambda}\,\mathrm{d}\lambda$$

Giving radiance as:

$$L(v) = \frac{P_{\mathrm{EL}}(v)}{A\Omega}$$

where A is the active area of the pixel, h is the Planck's constant and c is the velocity of light.

Determination of the exciton binding energy. This method of exciton binding energy determination can only be used by assuming that the depopulation of the photogenerated excitons is dominated by the thermal dissociation and radiative spontaneous emission processes[48].

The E_b value was extracted from temperature-dependent PL measurements. We assume that the measured PL arises from excitonic annihilations and that the decrease in the PL intensity is solely due to the increase in the thermal dissociation rate of excitons at higher temperatures[48]. The integrated PL intensity as a function of temperature could then be fitted through an Arrhenius equation:

$$I(T) = \frac{I_o}{1 + Ae^{(-E_b/k_B T)}}$$

where I_o is the low-temperature integrated PL intensity and k_B is the Boltzmann constant.

For the temperature-dependent PL measurements, the sample was kept in a liquid helium cryostat under vacuum. The temperature was collected from 300 to 40 K using a temperature controller. A home-built fluorescence spectrometer based on the 521 nm Ar-ion laser line as the excitation source was used. The PL intensity was measured in temperature steps of 20 K at the same spatial location on the sample. The temperature was stabilized for 10 min before each measurement. The corresponding PL raw spectra are shown in Supplementary Fig. 2a–d for $\langle n \rangle = \infty$, 10, 5, 3. The corresponding integrated intensities are plotted in Supplementary Fig. 2e

together with the Arrehenius fit profiles. The extracted E_b values and the temperature-dependent emission peak positions are also reported in Supplementary Fig. 2a,b, respectively.

References

45. de Mello, J., Wittmann, H. F. & Friend, R. H. An improved experimental determination of external photoluminescence quantum efficiency. *Adv. Mater.* **9,** 230–232 (1997).
46. Supran, G. J. *et al.* High-performance shortwave-infrared light-emitting devices using core–shell (PbS–CdS) colloidal quantum dots. *Adv. Mater.* **27,** 1437–1442 (2015).
47. Sun, L. *et al.* Bright infrared quantum-dot light-emitting diodes through inter-dot spacing control. *Nature Nanotech.* **7,** 369–373 (2012).
48. Chen, Z. *et al.* Photoluminescence study of polycrystalline $CsSnI_3$ thin films: determination of exciton binding energy. *J. Lumin.* **132,** 345–349 (2012).